Monthly Notices
of the
ROYAL ASTRONOMICAL SOCIETY

MNRAS **483,** 57–69 (2019)
Advance Access publication 2018 October 27

doi:10.1093/mnras/sty2918

A catalogue of nuclear stellar velocity dispersions of nearby galaxies from Hα STIS spectra to constrain supermassive black hole masses

Ilaria Pagotto [1]★ Enrico Maria Corsini [1,2] Marc Sarzi,[3,4] Bruno Pagani,[5] Elena Dalla Bontà [1,2] Lorenzo Morelli[6] and Alessandro Pizzella[1,2]

[1] *Dipartimento di Fisica e Astronomia 'G. Galilei', Università di Padova, vicolo dell'Osservatorio 3, I-35122 Padova, Italy*
[2] *INAF-Osservatorio Astronomico di Padova, vicolo dell'Osservatorio 2, I-35122 Padova, Italy*
[3] *Armagh Observatory and Planetarium, College Hill, Armagh BT61 9DG, UK*
[4] *Centre for Astrophysics Research, University of Hertfordshire, College Lane, Hatfield AL10 9AB, UK*
[5] *Département Sciences de la Matière, ENS de Lyon, 46 allée d'Italie, F-69364 Lyon, France*
[6] *Instituto de Astronomia y Ciencias Planetarias, Universidad de Atacama, Copayapu 485, 1530000 Copiapó, Chile*

Accepted 2018 October 8. in original form 2018 August 31

ABSTRACT

We present new measurements for the nuclear stellar velocity dispersion σ_* within subarcsecond apertures for 28 nearby galaxies. Our data consist of Space Telescope Imaging Spectrograph (STIS) long-slit spectra obtained with the G750M grating centred on the Hα spectral range. We fit the spectra using a library of single stellar population models and Gaussian emission lines, while constraining in most cases the stellar-population content from an initial fit to G430L STIS spectra. We illustrate how these σ_* measurements can be useful for constraining the mass $M_\bullet$ of supermassive black holes (SBHs) by concentrating on the cases of the lenticular galaxies NGC 4435 and NGC 4459. These are characterized by similar ground-based half-light radii stellar velocity dispersion σ_e values but remarkably different $M_\bullet$ as obtained from modelling their central ionized-gas kinematics, where NGC 4435 appears to host a significantly undermassive SBH compared to what is expected from the $M_\bullet - \sigma_e$ relation. For both galaxies, we build Jeans axisymmetric dynamical models to match the ground-based stellar kinematics obtained with Spectrographic Areal Unit for Research on Optical Nebulae integral-field spectrograph, including an SBH with $M_\bullet$ value as predicted by the $M_\bullet - \sigma_e$ relation and using high-resolution *HST* images taken with the Advanced Camera for Surveys to construct the stellar-mass model. By mimicking the *HST* observing conditions we use such reference models to make a prediction for the nuclear σ_* value. Whereas this was found to agree with our nuclear σ_* measurement for NGC 4459, for NGC 4435 the observed σ_* is remarkably smaller than the predicted one, which further suggests that this galaxy could host an undermassive SBH.

Key words: black hole physics – galaxies: fundamental parameters – galaxies: kinematics and dynamics – galaxies: photometry.

1 INTRODUCTION

Nowadays, there is a large body of evidence supporting the idea that a supermassive black hole (SBH), with a mass $M_\bullet$ ranging from 10^6 to 10^{10} $M_\odot$, lies in the centre of most of galaxies. Over the last two decades, the SBH mass was found to correlate with several properties of their host galaxy and, in particular, of its spheroidal component, which corresponds to the entire galaxy in the case of ellipticals or to the bulge for lenticulars and spirals. These correlations suggest that the SBHs and their host spheroids grew together, and since the slope and scatter of such correlations are thought to relate to the details of the SBH-galaxy coevolution, there is a constant demand for collecting $M_\bullet$ measurements across a large number of galaxies encompassing a wide range of host-galaxy masses and morphologies (see Kormendy & Ho 2013, for a review).

The relationship between $M_\bullet$ and the stellar velocity dispersion σ_* of the spheroidal component is currently the tightest correlation discovered so far (Beifiori et al. 2012; Kormendy & Ho 2013; van den Bosch 2016), although there are open issues about its slope (Saglia et al. 2016), whether the SBHs in barred and ordinary galaxies and/or classical and pseudobulges follow the same correlation

★ E-mail: ilaria.pagotto@phd.unipd.it

(Graham 2016), and the role of the over and undermassive SBHs with respect to those tracing the correlation (Savorgnan & Graham 2015; Krajnović et al. 2018). In fact, there is still the need of increasing the statistics of $M_\bullet$ in some specific physical ranges. Indeed, van den Bosch et al. (2015) and Shankar et al. (2016) showed that the available $M_\bullet$ estimates and their scaling relations suffer from a remarkable bias since less dense galaxies are underrepresented in the SBH demography. The variety of tracers, dynamical models, and algorithms adopted to recover the mass distribution in the centre of galaxies and constrain $M_\bullet$ is a further complication when building an unbiased sample. One significant contribution in this direction was given by the stringent $M_\bullet$ limits obtained for more than one hundred galaxies by Sarzi et al. (2002), Beifiori et al. (2009), and Pagotto et al. (2017), using nuclear line-width measurement for the nebular emission observed at sub-arcsecond resolution with the *Hubble Space Telescope* (*HST*).

Outlier galaxies with $M_\bullet$ far from the predictions of scaling relations represent an interesting challenge for understanding the co-evolution of galaxies and SBHs. High $M_\bullet$ outliers include NGC 4468b (Kormendy et al. 1997) and NGC 1277 (van den Bosch et al. 2012), which are characterized by a steep inward σ_* gradient with central values not consistent with the Faber–Jackson relation, NGC 4342 (Cretton & van den Bosch 1999), which is the strongest outlier in the $M_\bullet - M_{k,\mathrm{bulge}}$ correlation, NGC 1271 (Walsh et al. 2015) and MRK 1216 (Walsh et al. 2017), which have too large σ_* with respect to their *K*-band luminosity. The finding of low $M_\bullet$ outliers, or even ruling out the presence of an SBH is a more challenging task given to the detection threshold imposed by the angular resolution of present telescopes. Yet, remarkable low $M_\bullet$ outlier examples do exist, such as the radio-loud elliptical NGC 4335 (Verdoes Kleijn et al. 2002) and the barred lenticular NGC 4435 (Coccato et al. 2006), where $M_\bullet$ was constrained from the central ionized-gas kinematics observed with *HST*, or the lenticular NGC 4474 and elliptical NGC 4551, where stringent $M_\bullet$ limits were derived from stellar dynamical models and ground-based integral-field observations assisted by adaptive optics (Krajnović et al. 2018). The merging galaxies NGC 1316 (Nowak et al. 2008) and NGC 4382 (Gültekin et al. 2011) have also quite small $M_\bullet$ for their galaxy luminosities but in these cases it is not clear if this could be linked to the merger physics and to limitations in search techniques. From a theoretical perspective, models of SBH evolution (e.g. Volonteri, Natarajan & Gültekin 2011) predict that about 20 per cent of galaxies with masses between 10^9 and 10^{10} $\mathrm{M}_\odot$ should be characterized by $M_\bullet$ values critically below those predicted from present scaling relations. This is explained with an ineffective growth of the SBHs, which also could be ejected or not formed at all from the very beginning. Therefore, assessing the fraction of undermassive black holes in nearby galaxies is crucial to understand how the SBHs increased their mass and settled in galactic nuclei.

In this context, this paper provides a catalogue of new measurements of nuclear σ_* that can be useful for the purpose of constraining $M_\bullet$. The paper is organized as follows. We describe the sample selection in Section 2. We measure the nuclear σ_* of the sample galaxies from Space Telescope Imaging Spectrograph (STIS) spectra in Section 3. We study in more detail NGC 4435 and NGC 4459 in Section 4 to illustrate how combining Advanced Camera for Surveys (ACS) photometry along with Spectrographic Areal Unit for Research on Optical Nebulae (SAURON) integral-field spectroscopy can constrain $M_\bullet$. Finally, we present our conclusions in Section 5. We adopt $H_0 = 70\,\mathrm{km\,s^{-1}\ Mpc^{-1}}$, $\Omega_\mathrm{M} = 0.3$, and $\Omega_\Lambda = 0.7$ as cosmological parameters all through the paper.

2 SAMPLE SELECTION

In order to measure the nuclear σ_* in nearby galaxies, we looked in the Hubble Data Archive for all the STIS medium-resolution spectra that were obtained with the slit crossing the nucleus.

We first considered the archival spectra of galaxies obtained with the G430M grating, except for those already obtained by Krajnović & Jaffe (2004) who already measured the stellar velocity and velocity dispersion along the major axis of four early-type galaxies. Unfortunately, almost all the other spectra were heavily contaminated by strong and broad [O III]λλ4959, 5007 emission lines due to the presence of an active galactic nucleus (AGN) that prevented us from successfully measuring the stellar kinematics. We then looked for archival spectra obtained with the G750M grating, excluding also in this case the observations of Batcheldor et al. (2013) who already provided stellar kinematics measurements for 36 galaxies in the wavelength range centred on the Ca II absorption triplet at about 8500 Å. This initial pruning left us with the same sample of 177 galaxies compiled by Beifiori et al. (2009) for which the G750M grating was centred on the Hα line, to which we added nine more galaxies observed with STIS in the same wavelength range after 2009. Among these 186 objects we then excluded those with STIS spectra displaying a strong AGN emission and adopted a threshold for the signal-to-noise ratio in the stellar continuum at $S/N = 15$ per resolution element to perform reliable σ_* measurements.

This selection led to a final sample composed by 28 nearby galaxies ($D < 70$ Mpc), covering a wide range of morphological types (from E to Scd) and nuclear activities (Seyfert 2, LINERs, H II nuclei), which are listed in Table 1. Almost all of them were observed with the 0.″2-wide slit and this yielded nearly the same spectral resolution of the template spectra we used to measure the stellar kinematics (see Section 3.2 for details). We considered only two galaxies (IC 0342 and NGC 4736) observed with the 0.″1-wide slit, owing to the superb *S/N* of the data. All other archival G750M spectra obtained with the 0.″1-wide slit have *S/N* that is too low.

Finally, to help with our stellar kinematics extraction based on the G750M spectra we also looked in the Hubble Data Archive for similarly centred low-resolution G430L spectra for all our sample galaxies, since these spectra can provide useful constraints on the nuclear stellar population composition (see e.g. Sarzi et al. 2005 and Section 3.2). G430L spectra were found for 24 objects.

3 NUCLEAR STELLAR VELOCITY DISPERSION

3.1 Long-slit spectroscopy

We retrieved from the Hubble Data Archive the STIS spectra of the sample galaxies obtained with the G430L and G750M gratings through either the 0.″1 × 52″ or the 0.″2 × 52″ slit positioned on the galaxy nucleus. The detector was a SITe CCD with 1024 × 1024 pixel of 21 × 21 $\mu\mathrm{m}^2$. The G430L spectra covered the wavelength range between about 3000–5700 Å, whereas the G750M spectra were characterized by a wavelength range of either 6490–7050 or 6300–6865 Å, depending on the tilt angle of the grating. For the G750M spectra, the reciprocal dispersion was 0.554 and 1.108 Å pixel^{-1} for the 1-pixel and 2-pixel binning read-out mode along the dispersion direction, respectively. For an extended source, this setup yielded for the 0.″1-wide slit an instrumental full width at half-maximum (FWHM) of 5.5 and 1.1 Å with the G430L and G750M grating, respectively, and it yielded for the 0.″2-wide slit 10.9 and 2.2 Å with the G430L and G750M grating, respectively

Table 1. Properties of the sample galaxies.

					G430L						G750M							
Galaxy	Morph.	Sp. Cl.	D	Prop. Id.	PA	Exp. Time	SP. Range	Bin.	Apert.		Prop. Id.	PA	Exp. Time	SP. Range	Bin.	Apert.		$\sigma_{*,\mathrm{fix}}$	$\sigma_{*,\mathrm{free}}$
			(Mpc)		(°)	(h)	(Å)		(″)	(pc)		(°)	(h)	(Å)		(″)	(pc)	(km s^{-1})	(km s^{-1})
(1)	(2)	(3)	(4)	(5)	(6)	(7)	(8)	(9)	(10)	(11)	(12)	(13)	(14)	(15)	(16)	(17)	(18)	(19)	(20)
IC0342	SABcd(rs)	H	4.3	–	–	–	–	–	–	–	8591	13.9	0.80	6300–6865	1 × 1	0.1 × 0.15	2 × 3	–	$53.9^{+7.8}_{-3.8}$
NGC 2685	(R)SB0$^+$pec	S2/T2:	14.3	8607	54.4	0.72	3000–5700	1 × 2	0.2 × 0.30	14 × 21	8607	54.4	0.86	6300–6865	1 × 2	0.2 × 0.30	14 × 21	$62.7^{+8.8}_{-7.8}$	$51.0^{+9.7}_{-8.3}$
NGC 3245	SA0^0(r):?	T2:	23.2	–	–	–	–	–	–	–	7403	2.4	0.75	6300–6865	1 × 1	0.2 × 0.25	22 × 28	–	$260.4^{+29.2}_{-23.5}$
NGC 3368	SABab(rs)	L2	17.8	7361	69.5	0.44	3000–5700	1 × 1	0.2 × 0.25	17 × 22	7361	69.5	0.75	6300–6865	1 × 1	0.2 × 0.25	17 × 22	$93.4^{+6.4}_{-6.1}$	$103.9^{+7.9}_{-4.7}$
NGC 3379	E1	L2/T2::	18.0	–	–	–	–	–	–	–	8589	75.3	1.78	6300–6865	1 × 1	0.2 × 0.25	17 × 22	–	$264.7^{+29.6}_{-42.5}$
NGC 3489	SAB0$^+$(rs)	T2/S2	14.6	7361	59.1	0.46	3000–5700	1 × 1	0.2 × 0.25	14 × 18	7361	59.1	0.71	6300–6865	1 × 1	0.2 × 0.25	14 × 18	$74.1^{+3.9}_{-4.0}$	$78.2^{+2.4}_{-3.5}$
NGC 3627	SABb(s)	T2/S2	15.4	8607	80.1	0.65	3000–5700	1 × 2	0.2 × 0.30	15 × 22	8607	80.1	0.79	6300–6865	1 × 2	0.2 × 0.30	15 × 22	$114.3^{+18.5}_{-13.6}$	–
NGC 3675	SAb(s)	T2	14.4	8607	25.9	0.69	3000–5700	1 × 2	0.2 × 0.30	14 × 21	8607	25.9	0.83	6300–6865	1 × 2	0.2 × 0.30	14 × 21	$110.7^{+13.7}_{-11.1}$	$115.5^{+8.1}_{-17.2}$
NGC 3992	SBbc(rs)	T2:	17.5	7361	155.3	0.50	3000–5700	1 × 1	0.2 × 0.25	17 × 21	7361	155.3	0.82	6300–6865	1 × 1	0.2 × 0.25	17 × 21	$145.9^{+13.1}_{-13.3}$	$146.1^{+14.3}_{-11.9}$
NGC 4030	SAbc(s)	H*	26.1	9783	90.7	0.61	3000–5700	1 × 1	0.2 × 0.25	25 × 32	8228	42.1	0.24	6490–7050	2 × 2	0.2 × 0.30	25 × 38	$82.3^{+27.7}_{-26.8}$	$87.4^{+18.1}_{-16.6}$
NGC 4245	SB0/a(r):	H	16.7	7361	85.7	0.46	3000–5700	1 × 1	0.2 × 0.25	16 × 20	7361	85.7	0.75	6300–6865	1 × 1	0.2 × 0.25	16 × 20	$83.8^{+7.2}_{-7.0}$	$75.6^{+5.3}_{-4.6}$
NGC 4314	SBa(rs)	L2	17.8	7361	105.3	0.46	3000–5700	1 × 1	0.2 × 0.25	17 × 22	7361	105.3	0.75	6300–6865	1 × 1	0.2 × 0.25	17 × 22	$78.2^{+9.3}_{-7.3}$	$69.8^{+9.8}_{-6.5}$
NGC 4321	SABbc(s)	T2	27.1	7361	92.9	0.46	3000–5700	1 × 1	0.2 × 0.25	26 × 33	7361	92.9	0.74	6300–6865	1 × 1	0.2 × 0.25	26 × 33	$56.9^{+12.3}_{-12.2}$	$61.3^{+11.5}_{-12.9}$
NGC 4414	SAc(rs)?	T2:	14.2	8607	125.1	0.67	3000–5700	1 × 2	0.2 × 0.30	14 × 21	8607	125.1	0.81	6300–6865	1 × 2	0.2 × 0.30	14 × 21	$82.4^{+3.9}_{-3.3}$	$85.2^{+3.7}_{-7.8}$
NGC 4429	SA0$^+$(r)	T2	20.5	8607	81.1	0.65	3000–5700	1 × 2	0.2 × 0.30	20 × 30	8607	81.1	0.79	6300–6865	1 × 2	0.2 × 0.30	20 × 30	$213.2^{+22.3}_{-18.3}$	$201.7^{+22.6}_{-21.2}$
NGC 4435	SB0^0(s)	T2/H:	16.0	7361	89.6	0.46	3000–5700	1 × 1	0.2 × 0.25	20 × 25	7361	89.6	0.74	6300–6865	1 × 1	0.2 × 0.25	20 × 25	$87.3^{+10.2}_{-8.8}$	$95.0^{+10.9}_{-9.4}$
NGC 4459	SA0$^+$(r)	T2:	21.7	7361	92.9	0.46	3000–5700	1 × 1	0.2 × 0.25	21 × 26	7361	92.9	0.74	6300–6865	1 × 1	0.2 × 0.25	21 × 26	$214.6^{+11.2}_{-12.0}$	$200.2^{+12.5}_{-10.2}$
NGC 4477	SB0(s):?	S2	23.8	7361	92.8	0.46	3000–5700	1 × 1	0.2 × 0.25	23 × 29	7361	92.8	0.73	6300–6865	1 × 1	0.2 × 0.25	23 × 29	$154.4^{+15.2}_{-11.5}$	$158.4^{+11.2}_{-18.2}$
NGC 4501	SAb(rs)	S2	37.2	7361	91.9	0.46	3000–5700	1 × 1	0.2 × 0.25	36 × 45	7361	91.9	0.74	6300–6865	1 × 1	0.2 × 0.25	36 × 45	$102.4^{+12.3}_{-10.5}$	$91.5^{+13.2}_{-14.8}$
NGC 4548	SBb(rs)	L2	11.5	7361	73.2	0.46	3000–5700	1 × 1	0.2 × 0.25	11 × 14	7361	73.2	0.74	6300–6865	1 × 1	0.2 × 0.25	11 × 14	$79.8^{+11.5}_{-8.9}$	$81.0^{+10.2}_{-11.5}$
NGC 4596	SB0$^+$(r)	L2::	31.7	7361	70.3	0.46	3000–5700	1 × 1	0.2 × 0.25	31 × 38	7361	70.3	0.75	6300–6865	1 × 1	0.2 × 0.25	31 × 38	$219.1^{+20.0}_{-15.5}$	$210.3^{+19.4}_{-14.8}$
NGC 4698	SAab(s)	S2	19.1	7361	79.0	0.46	3000–5700	1 × 1	0.2 × 0.25	19 × 23	7361	79.0	0.74	6300–6865	1 × 1	0.2 × 0.25	19 × 23	$114.9^{+9.9}_{-9.8}$	$109.7^{+10.3}_{-9.8}$
NGC 4736	(R)SAab(r)	L2	7.6	–	–	–	–	–	–	–	8591	50.1	1.09	6300–6865	1 × 1	0.1 × 0.15	4 × 6	–	$109.9^{+4.8}_{-7.0}$
NGC 4800	SAb(rs)	H	15.5	7361	177.5	0.48	3000–5700	1 × 1	0.2 × 0.25	15 × 19	7361	177.5	0.80	6300–6865	1 × 1	0.2 × 0.25	15 × 19	$89.5^{+7.2}_{-7.6}$	$86.6^{+10.5}_{-7.2}$
NGC 4826	(R)SAab(rs)	T2	10.0	8607	88.1	0.65	3000–5700	1 × 2	0.2 × 0.30	10 × 15	8607	88.1	0.80	6300–6865	1 × 2	0.2 × 0.30	10 × 15	$82.0^{+6.5}_{-5.9}$	$82.7^{+6.1}_{-3.7}$
NGC 5055	SAbc(rs)	T2	9.8	7361	164.5	0.47	3000–5700	1 × 1	0.2 × 0.25	9 × 12	7361	164.5	0.79	6300–6865	1 × 1	0.2 × 0.25	9 × 12	$104.3^{+4.9}_{-5.1}$	$111.1^{+2.0}_{-1.0}$
NGC 7252	(R)SA0^0:	H*	64.1	7435	38.1	4.25	3000–5700	1 × 2	0.1 × 0.10	31 × 31	8669	126.1	0.19	6490–7050	2 × 2	0.2 × 0.30	62 × 93	$74.4^{+13.0}_{-11.4}$	$77.5^{+14.0}_{-11.5}$
NGC 7331	SAb(s)	T2	7.0	8607	178.9	0.67	3000–5700	1 × 2	0.2 × 0.30	7 × 10	8607	178.9	0.81	6300–6865	1 × 2	0.2 × 0.30	7 × 10	$118.9^{+6.7}_{-6.3}$	$115.8^{+10.5}_{-6.3}$

Notes. Col.(1): galaxy name. Col.(2): morphological type from de Vaucouleurs et al. (1991, RC3). Col.(3): nuclear spectral class (Ho, Filippenko & Sargent 1997), where S = Seyfert, L = LINER, H = H II nucleus, T = transition object (LINER/H II), and 2 = type 2. Classifications evaluated as uncertain or highly uncertain are marked with a single or double colon, respectively. Classifications marked with * are from NASA/IPAC Extragalactic Database (NED). Col.(4): distance from NED. The distances are obtained as $D = V_{3K}/H_0$, where V_{3K} is the weighted mean recessional velocity corrected to the reference frame of the microwave background radiation and $H_0 = 70\,\mathrm{km\,s^{-1}\,Mpc^{-1}}$. For IC 0342 we assume the distance reported in Beifiori et al. (2009) and rescaled for $H_0 = 70\,\mathrm{km\,s^{-1}\,Mpc^{-1}}$ since V_{3K} is not provided by NED. Col(5): *HST* proposal number for the G430L spectra. Col.(6): position angle of the slit for the G430L spectra. Col.(7): total exposure time for the G430L spectra. Col.(8): spectral range for the G430L spectra. Col.(9): pixel binning for the G430L spectra. Col.(10): size of the nuclear aperture within which the fit was performed for the G430L spectra. Col.(11): physical size of the nuclear aperture within which the fit was performed for the G430L spectra. Col.(12): *HST* proposal number for the G750M spectra. Col.(13): position angle of the slit for the G750M spectra. Col.(14): total exposure time for the G750M spectra. Col.(15): spectral range for the G750M spectra. Col.(16): pixel binning for the G750M spectra. Col.(17): size of the nuclear aperture within which the fit was performed for the G750M spectra. Col.(18): physical size of the nuclear aperture within which the fit was performed for the G750M spectra. Col.(19): nuclear σ_* obtained using the G430L optimal template when fitting the G750M spectra. Col.(20): nuclear σ_* obtained without using the G430L optimal template when fitting the G750M spectra.

(Riley et al. 2017). The spatial scale was 0.″0507 and 0.″101 pixel^{-1} for the 1-pixel and 2-pixel binning read-out mode along the spatial direction, respectively. The proposal number, slit width, and position angle, pixel binning, wavelength range, and total exposure times of the STIS spectra of the sample galaxies are reported in Table 1.

We reduced the spectra as done in Beifiori et al. (2009) and Pagotto et al. (2017). We used both IRAF[1] tasks and STIS reduction pipeline (Dressel, Holfeltz & Quijano 2007), which we combined in a customized IRAF procedure running the `lacos_spec` task (van Dokkum 2001) to remove the cosmic rays events or hot pixels. The reduction steps included the subtraction of the overscan, bias, and dark contributions, correction for internal flat-field, trimming of the spectra, removal of bad pixels and cosmic rays, wavelength and flux calibration, correction for geometrical distortion, alignment, and combination of the spectra obtained for the same galaxy with the same setup. Finally, we averaged the innermost spectral rows of each resulting spectrum for the purpose of analysing a nearly squared aperture as prescribed by Beifiori et al. (2009).

3.2 Stellar kinematics

We measured the nuclear σ_* with the Penalized Pixel Fitting (PPXF, Cappellari & Emsellem 2004) and the Gas and Absorption Line Fitting (GANDALF, Sarzi et al. 2006) IDL[2] algorithms. In both instances, to model the stellar continuum we used the library of synthetic spectral energy distributions (SEDs) for single-age, single-metallicity stellar populations provided by Vazdekis et al. (2010), which is based on the Medium Resolution Isaac Newton Telescope Library of Empirical Spectra (MILES, Sánchez-Blázquez et al. 2006) and covers the full optical spectral range of both our G430L and G750M STIS spectra at moderately high resolution (*FWHM* =2.5 Å, Falcón-Barroso et al. 2011).

The fitting procedure consists of the following steps. We first rebinned each galaxy spectrum and MILES SED template along the dispersion direction to a common logarithmic scale. For each galaxy, we then run a preliminary fit to its STIS G750M spectrum using PPXF while masking the emission lines and considering a Gaussian LOSVD in order to obtain a starting guess on both velocity and σ_*. We then run a series of GANDALF fits to the nuclear spectrum while optimizing the values for the velocity and σ_* that GANDALF takes as input using a downhill simplex method (AMOEBA, Nelder & Mead 1965). This optimization yields a final GANDALF fit and best velocity and σ_* values, as well as an initial estimate for the errors on these parameters. These error estimates are then refined by means of a grid of GANDALF models based on velocity and σ_* values around the previously found best-fitting results. When necessary we also included a broad-line emission component in our GANDALF fits.

It should be noticed that the spectral resolution of the MILES SEDs is somewhat poorer than that of the G750M ones. The MILES resolution, near the Hα line corresponds to an instrumental velocity dispersion $\sigma_{\rm inst}$ of about 49 km s^{-1} whereas for the G750M spectra $\sigma_{\rm inst} = 21$ and 43 km s^{-1} for the 0.″1 and 0.″2-wide slit, respectively. During our PPXF and GANDALF fits we decided against degrading the resolution of our G750M spectra, since this would artificially smooth our spectra and lead to less reliable error estimates. Instead, we corrected the measured σ_* to account for the mismatch between the instrumental resolution of our G750M data and the MILES templates, by summing such a difference in quadrature to our best-fitting σ_* values. Such a correction is quite significant for 0.″1-wide slit spectra (ranging from 16 to 8 km s^{-1} for original σ_* estimates of 50 and 100 km s^{-1}, respectively) whereas it remains quite small for the 0.″2-wide slit ones (ranging from 5 to less than 3 km s^{-1} in the same range).

For the 24 sample galaxies with a G430L spectrum, we further refit the G750M spectrum drawing from the results of a previous fit to the G430L spectra in order to better constrain the stellar-population content of the nuclear regions. More specifically, we performed a GANDALF fit to determine the weights of the best-fitting linear combination of MILES SEDs when modelling the G430L spectra and use these to construct an optimal stellar-population template that, in turn, can be used in our GANDALF fit to the G750M spectra. As in the case of the G430L the spectral resolution is significantly worse than that of the MILES SEDs (which is also the reason why the G430L cannot be used to measure σ_* in first place), we proceeded to degrade the resolution of the latter templates to match that of G430L spectra before the fit, as it is common practice in these cases.

Figs 1 and 2 illustrate for four sample objects both the quality of our GANDALF fit to the G750M spectra as well as the working of our error estimation. For NGC 4736 the GANDALF fit employs the whole library of MILES SEDs, whereas all other examples correspond to fit based on the previously derived G430L optimal template. In this respect, Fig. 3 shows the comparison between the values $\sigma_{*,\rm fix}$ of the nuclear velocity dispersion obtained from the G750M spectra adopting the G430L optimal templates and values $\sigma_{*,\rm free}$ measured from G750M spectra using the entire MILES SED library, for all but one of the 24 objects with both G430L and G750M spectra (for NGC 3627 only the fit adopting the optimal template was successful). In addition to these, in Fig. 3 we also add NGC 3245 and NGC 3379 for which we adopted as G430L optimal template the built by averaging those from the fit to NGC 4429, NGC 4459, and NGC 4596. This is appropriate since there are good indications that both NGC 3245 and NGC 3379 host central old stellar population (Kuntschner et al. 2010; McDermid et al. 2015) as indicated by the stellar-population mix returned in the case of the G430L fits to NGC 4429, NGC 4459, and NGC 4596. We found $\sigma_{*,\rm fix} = 274.4^{+29.3}_{-23.3}$ km s^{-1} for NGC 3245 and $\sigma_{*,\rm fix} = 242.1^{+35.3}_{-21.0}$ km s^{-1} for NGC 3379. Fig. 3 shows that the values of $\sigma_{*,\rm fix}$ and $\sigma_{*,\rm free}$ are consistent with each other within 1σ errors in almost all cases (see also Table 1), which gives us confidence in the $\sigma_{*,\rm free}$ obtained for those objects (IC 0342, NGC 3245, NGC 3379, and NGC 4736) for which G430L spectra are not available.

Batcheldor et al. (2013) already measured the nuclear σ_* of NGC 4736, NGC 4826, and NGC 5055 from G750M spectra and 0.″1-wide slit in the wavelength range centred on the Ca II absorption triplet at about 8500 Å. This allowed us to make a comparison between σ_* obtained on sub-arcsecond apertures from G750M spectra in different wavelength ranges and with a different fitting technique. To this aim, we re-extracted the nuclear spectra of these galaxies in apertures matching as much as possible that of Batcheldor et al. (2013, 0.″1 × 0.″05) and repeated the fit. For NGC 4736, we were able to match the aperture and found $\sigma_{*,\rm free} = 111.5^{+6.5}_{-10.6}$ km s^{-1}. For NGC 4826 and NGC 5055, we could analyse only a wider aperture since our G750M spectra were taken with the 0.″2-wide slit. From the spectra extracted from the smallest possible aperture (0.″2 × 0.″1 for NGC 4826 and 0.″2 × 0.″05 for NGC 5055), we measured $\sigma_{*,\rm fix} = 75.1^{+8.9}_{-9.0}$ km s^{-1} for NGC 4826 and a $\sigma_{*,\rm fix} = 93.6^{+5.5}_{-5.6}$ km s^{-1} for

[1]Image Reduction and Analysis Facility is distributed by the National Optical Astronomy Observatory (NOAO), which is operated by the AURA, Inc., under cooperative agreement with the National Science Foundation.
[2]Interactive Data Language is distributed by Harris Geospatial Solutions.

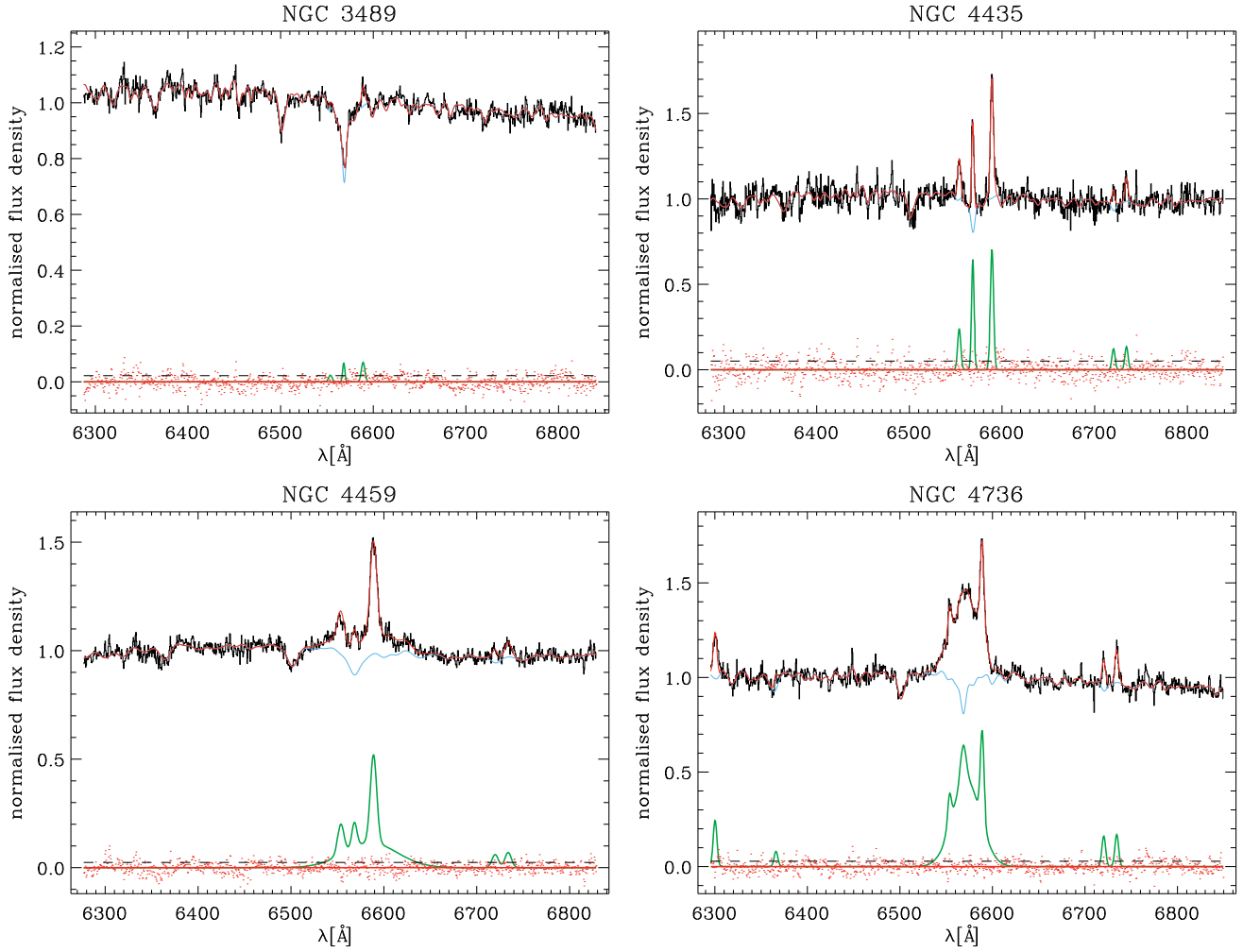

Figure 1. Examples of rest-frame G750M spectra covering different cases with very weak narrow emission lines, bright narrow emission lines only, bright narrow and broad emission lines. The galaxy name is given in each panel and the relative fluxes have false zero points for viewing convenience. The best-fitting model (red line) is the sum of the spectra of the ionized-gas (green line) and stellar component (cyan line). The latter is obtained by convolving the synthetic templates with the best-fitting LOSVD and multiplying them by the best-fitting Legendre polynomials. The residuals (red dots) are obtained by subtracting the model from the spectrum. The dashed line corresponds to the rms of the residuals.

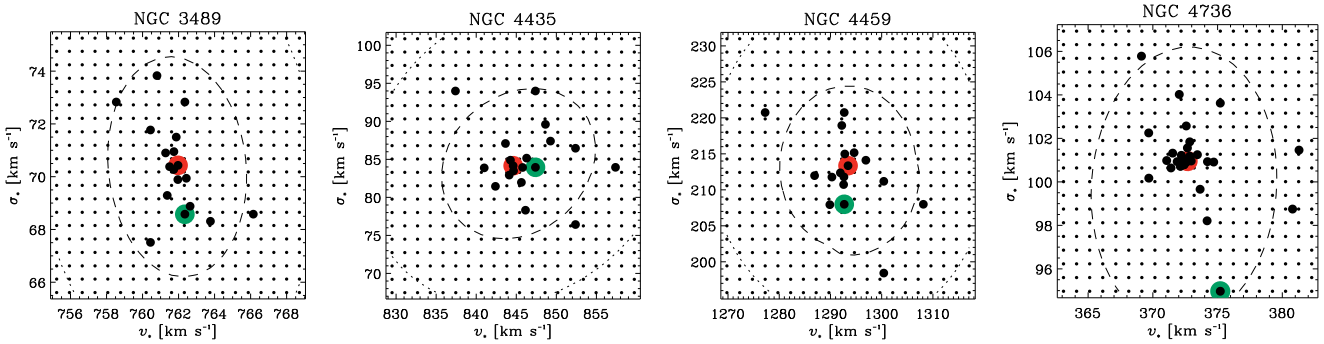

Figure 2. Grid of GANDALF models of the G750M spectra of NGC 3489, NGC 4435, NGC 4459, and NGC 4736 (*from left to right*) for different velocities and velocity dispersions of the stellar component (black small circles). The final best-fitting GANDALF model is shown with a big red circle while the starting best-fitting PPXF model is shown with a big green circle. Big black circles correspond to AMOEBA iterations. Contours show the distribution of $\Delta\chi^2 = \chi^2 - \chi^2_{\rm min}$ with the dashed and dotted lines indicating the 1σ and 2σ confidence level for two degrees of freedom, respectively.

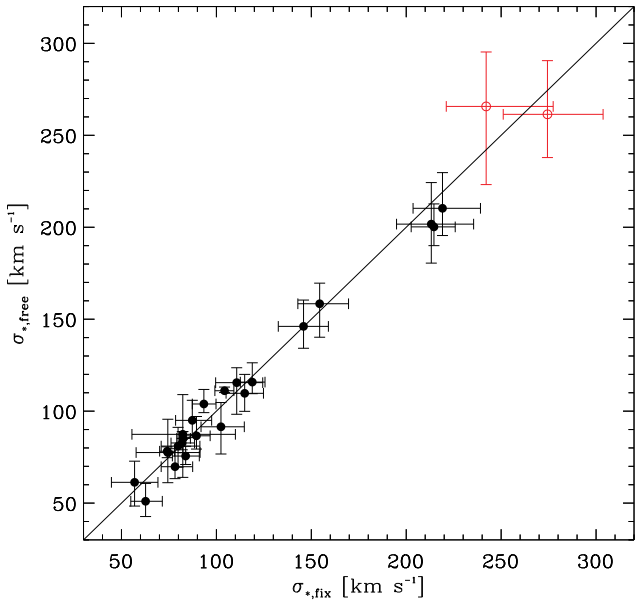

Figure 3. Comparison between the values of $\sigma_{*,\rm fix}$ and $\sigma_{*,\rm free}$ obtained from the G750M spectra of 23 sample galaxies (black filled circles) with and without adopting the optimal template from the G430L spectra, respectively. The $\sigma_{*,\rm fix}$ values of NGC 3245 and NGC 3379 (red open circles), for which no G430L spectrum was available, were obtained by averaging the optimal templates of NGC 4429, NGC 4459, and NGC 4596.

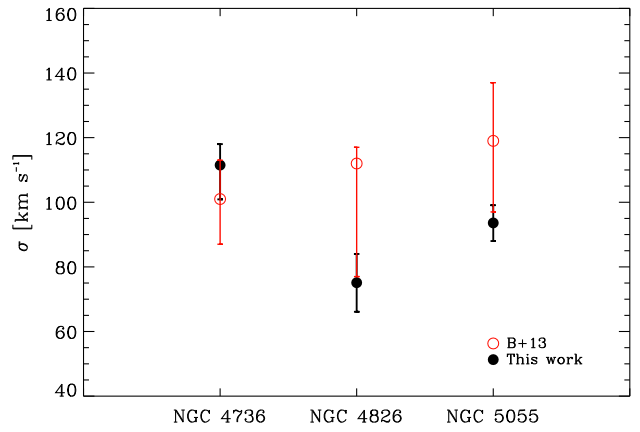

Figure 4. Comparison between our sub-arcsecond σ_* measurements of NGC 4736, NGC 4826, and NGC 5055 from G750M spectra in the Hα region (black filled circles) and those by Batcheldor et al. (2013) (red open circles) from G750M spectra centred on the Ca II absorption triplet at about 8500 Å.

NGC 5055. Our measurements are in agreement with those by Batcheldor et al. (2013) within the 1σ error bars (Fig. 4).

4 STELLAR DYNAMICAL MODELS FOR NGC 4435 AND NGC 4459

In this section we focused on the particular cases of NGC 4435 and NGC 4459 since these have very similar ground-based but quite different STIS measurements of σ_*, which in turn may be indicative of a significantly different $M_\bullet$ at a given, similar bulge mass.

Indeed, whereas the values for $\sigma_{\rm e}$ (the stellar velocity dispersion measured within a circular aperture corresponding to the galaxy effective radius $r_{\rm e}$) obtained by Cappellari et al. (2013) using SAURON integral-field spectroscopy are fairly similar for these two galaxies (amounting to $\sigma_{\rm e} = 152.8 \pm 7.6$ and 158.1 ± 7.9 km s^{-1} for NGC 4435 and NGC 4459, respectively), our STIS measurements return a much smaller $\sigma_{*,\rm fix}$ value for NGC 4435 than for NGC 4459 (amounting to $87.3^{+10.2}_{-8.8}$ and $214.6^{+11.2}_{-12.0}$ km s^{-1}, respectively, see Table 1). In fact, the nuclear σ_* value for NGC 4435 is also at odds with what is expected from the aperture velocity dispersion correction for early-type galaxies of Falcón-Barroso et al. (2017), which for a $r_{\rm e} = 23\farcs5$ would lead to a σ_*=203.7 $\pm$ 10.1 km s^{-1}. On the other hand, for NGC 4459 and a $r_{\rm e} = 43\farcs1$ the same aperture correction returns a σ_*=217.9 $\pm$ 10.8 km s^{-1} that is entirely consistent with our actual STIS measurement. Although the use of such an aperture correction down to sub-arcsecond scales represents almost an extrapolation, given that the work of Falcón-Barroso et al. (2017) is based on ground-based data, the previous comparison further suggests that NGC 4435 and NGC 4459 have very different central stellar kinematics. As to whether this may indicate a different black hole mass budget, we note that gas-dynamical $M_\bullet$ measurements already point in this direction. Indeed, whereas NGC 4459 shows an $M_\bullet$ value consistent with the $M_\bullet - \sigma_\star$ relation (Sarzi et al. 2001), the $M_\bullet$ of NGC 4435 falls significantly below it (Coccato et al. 2006) in spite of their similar $\sigma_{\rm e}$ values.

Given these indications, we decided to use the cases of NGC 4435 and NGC 4459 to explore how our STIS sub-arcsecond σ_* measurements can be used to constrain the central mass concentration of galaxies, in particular when large integral-field spectroscopic measurements are available to provide further constraints on the stellar motions. To this goal, in what follows we describe how we proceeded to deproject the stellar surface-brightness distribution to obtain the galaxy luminosity density with the multi-Gaussian expansion (MGE) method of Emsellem, Monnet & Bacon (1994) and how we built a stellar dynamical model using the Jeans axisymmetric modelling (JAM) algorithm of Cappellari (2008), while assuming the $M_\bullet$ value predicted by the $M_\bullet - \sigma_{\rm e}$ relation and by matching the SAURON stellar kinematic maps provided by Krajnović et al. (2011).

4.1 Properties of NGC 4435

NGC 4435 is a barred lenticular galaxy at a distance $D = 16.0$ Mpc with a central nebular activity of intermediate type between that of LINERs and H II nuclei (Table 1). It is a member of the Virgo cluster (Binggeli, Sandage & Tammann 1985) and has an absolute total corrected B magnitude $M^0_{B_{\rm T}} = -19.41$ mag, as obtained from $B_{\rm T} = 11.74$ mag (RC3).

Although the proximity to the highly disturbed spiral NGC 4438 and the presence of optical plume that appears to connect NGC 4438 to NGC 4435 initially lead to suggest that these two galaxies are currently interacting (Vollmer et al. 2005), subsequent works indicate instead that NGC 4435 is relatively undisturbed. Kenney et al. (2008) indeed found that NGC 4438 has in fact collided with the nearby elliptical M86, whereas Cortese et al. (2010) interpreted the optical plume between NGC 4438 and NGC 4435 as due to Galactic cirrus.

NGC 4435 has boxy isophotes out to about 10″ from the centre and discy isophotes outwards. It hosts an inclined dust disc with blue star forming regions in the innermost 4″ from the centre (Ferrarese et al. 2006). Coccato et al. (2006) measured an upper limit of $M_\bullet < 7.5 \times 10^6\,{\rm M}_\odot$ from the modelling of resolved, ionized-gas kinematics based on STIS observations along various slit directions

and pointed out how this $M_\bullet$ value is far below the prediction of the $M_\bullet - \sigma_\star$ relation.

4.2 Properties of NGC 4459

NGC 4459 is an unbarred lenticular at a distance $D = 21.7$ Mpc with a central LINER/H II nebular activity (Table 1) belonging to the Virgo cluster (Binggeli et al. 1985). It has $M^0_{B_T} = -20.47$ mag from $B_T = 11.32$ mag (RC3). The early-type morphology of this galaxy was investigated by several authors by performing a photometric decomposition. Kormendy et al. (2009) fitted the *V*-band surface-brightness radial profile along the major axis of NGC 4459 with a Sérsic law and classified it as an elliptical galaxy. A Sérsic profile was also adopted by Vika et al. (2012) and Beifiori et al. (2012) in their 2D fit of the UKIDSS *K*-band and SDSS *i*-band images of the galaxy, respectively. On the contrary, Sani et al. (2011) and Savorgnan & Graham (2016) considered an exponential disc in addition to the Sérsic bulge in their photometric decomposition of the Spitzer 3.6-μm image. In their decomposition, Savorgnan & Graham (2016) pointed out that the disc starts to dominate the surface brightness profile for radii larger than 100″. The galaxy has regular elliptical isophotes although it hosts a dust disc that is extended out to about 8.″5 from the centre and characterized by clumps of star formation (Ferrarese et al. 2006). From the STIS kinematics of the ionized gas Sarzi et al. (2001) measured an $M_\bullet = 9.4 \times 10^7\,M_\odot$ by assuming an inclination $i = 47^\circ$ for the gaseous disc. This inclination value was determined by fitting ellipses to the innermost dust lanes, and is consistent with that found by Cappellari et al. (2007) based on stellar-dynamical models.

4.3 Broad-band photometry

In order to build a stellar-mass model for NGC 4435 and NGC 4459 and in turn dynamical models capable of constraining $M_\bullet$ using our nuclear σ_* measurements, we need both high-spatial resolution and wide-field images. Therefore, for both galaxies we retrieved Wide Field Camera (WFC) images (Prop. Id. 9401, P.I. Patrick Côté) obtained with the F850LP filter by ACS (Lucas et al. 2016) from the Hubble Legacy Archive. The available ACS/WFC frames were already reduced and combined with the Python tool `DrizzlePac` (Gonzaga et al. 2012). The final image is characterized by a field of view of 202″ × 202″ and a plate scale of 0.″049 pixel^{-1}. The images were oriented with north at the top and east to the left and given in electrons per second.

We flux calibrated the F850LP images in the AB photometric system as follows:

$$\mu = -2.5 \log\left(\frac{I}{G \cdot s^2}\right) + z_{\rm cal} - A_z, \quad (1)$$

where I is the surface brightness of each pixel in units of electrons per second, G is the gain in electrons per ADU, s is the plate scale in arcsec pixel^{-1}, $z_{\rm cal}$ is the calibration constant from the header of the images, and A_z is the Galactic extinction by Schlafly & Finkbeiner (2011). It is $G = 1$ electrons per ADU and $z_{\rm cal} = 24.871$ mag for both galaxies whereas it is $A_z = 0.036$ and 0.057 mag for NGC 4435 and NGC 4459, respectively. We converted the resulting surface brightness into the luminosity surface density in solar units using $M_{\odot,z} = 4.52$ mag for the z-band absolute AB magnitude of the Sun.

We subtracted the sky level tabulated in Pavlovsky et al. (2004). For each galaxy, we did a sanity check by comparing the given value with the mean value of the sky level we determined in a large number of 5 × 5 pixel areas of the image using the `imexamine` task in IRAF. We selected these areas in apparently empty regions far from the galaxy, which we considered free of objects to avoid the contamination of the light of field stars and galaxies, as well as of the target galaxy itself. For the estimated sky value and its error we adopted the average and rms of the mean values, respectively. The estimated sky value of NGC 4435 is consistent with that of Pavlovsky et al. (2004). On the contrary, our estimated sky level of NGC 4459 is significantly larger than that by Pavlovsky et al. (2004), suggesting that the light contribution of the galaxy nearly extends out to the edge of the field of view.

4.4 Dust masking

As both galaxies display prominent dust lanes in their central regions, we needed to account for their presence when fitting the surface brightness distribution. First, we carefully inspected the distribution of the dust to identify the regions where it may affect the surface brightness analysis. Indeed, NGC 4435 harbours a highly inclined disc of dust near the centre, while NGC 4459 has a more extended dust disc with the outer parts following the surface brightness distribution and the inner ones displaying a more irregular pattern (Fig. 5).

Ferrarese et al. (2006) performed a correction for dust absorption for NGC 4435, but they failed in recovering the surface brightness profile within the inner 2.″0. The dust disc can still be seen in the corrected image by Coccato et al. (2006) too, although it is less optically thick than in the uncorrected image. Ferrarese et al. (2006) considered their dust correction of NGC 4459 out to 7.″5 from the centre as not reliable. Therefore, we preferred to mask the dusty regions on the images of galaxies rather than correcting them. In both cases, the mask has the shape of half elliptical annulus with an ellipticity $\varepsilon = 1 - \cos i$ given by the inclination of the dust disc. This was measured by Coccato et al. (2006) and Ferrarese et al. (2006) for NGC 4435 ($i = 70^\circ$) and NGC 4459 ($i = 45^\circ$), respectively (Fig. 5). To define the location and size of the masked region and verify whether the galaxy centre was obscured, we compared the surface brightness measured in each pixel of the central portion of the image as a function of the distance from the galaxy centre.

The mask of NGC 4435 extends between 0.″1 and 4″ along the galaxy major axis. The resulting surface brightness profile reveals a lack of dust in the inner 0.″1. In fact, the unmasked pixels on the unobscured northwestern side of the galaxy have systematically a brighter surface brightness than those on the dusty southeastern side (Fig. 5).

The fact that the outer parts of the dust disc of NGC 4459 follow the surface brightness distribution made not possible to clearly distinguish obscured and unobscured pixels as we did in the previous case. We chose to mask only the galaxy portion where the dust absorption was stronger and more irregular. Therefore, we masked the northeastern half between 0.″4 and 3″ along the galaxy major axis since there were a few dust-affected pixels in the innermost region (Fig. 5).

4.5 Multi-Gaussian expansion analysis

In order to obtain a model for the luminosity volume density of both NGC 4435 and NGC 4459, and in turn for their mass density and gravitational potential, we started by parametrizing the surface brightness of the sky-subtracted and dust-masked image of each galaxy as the sum of a set of Gaussian components by using the MGE IDL algorithm by Cappellari (2002). The MGE method indeed

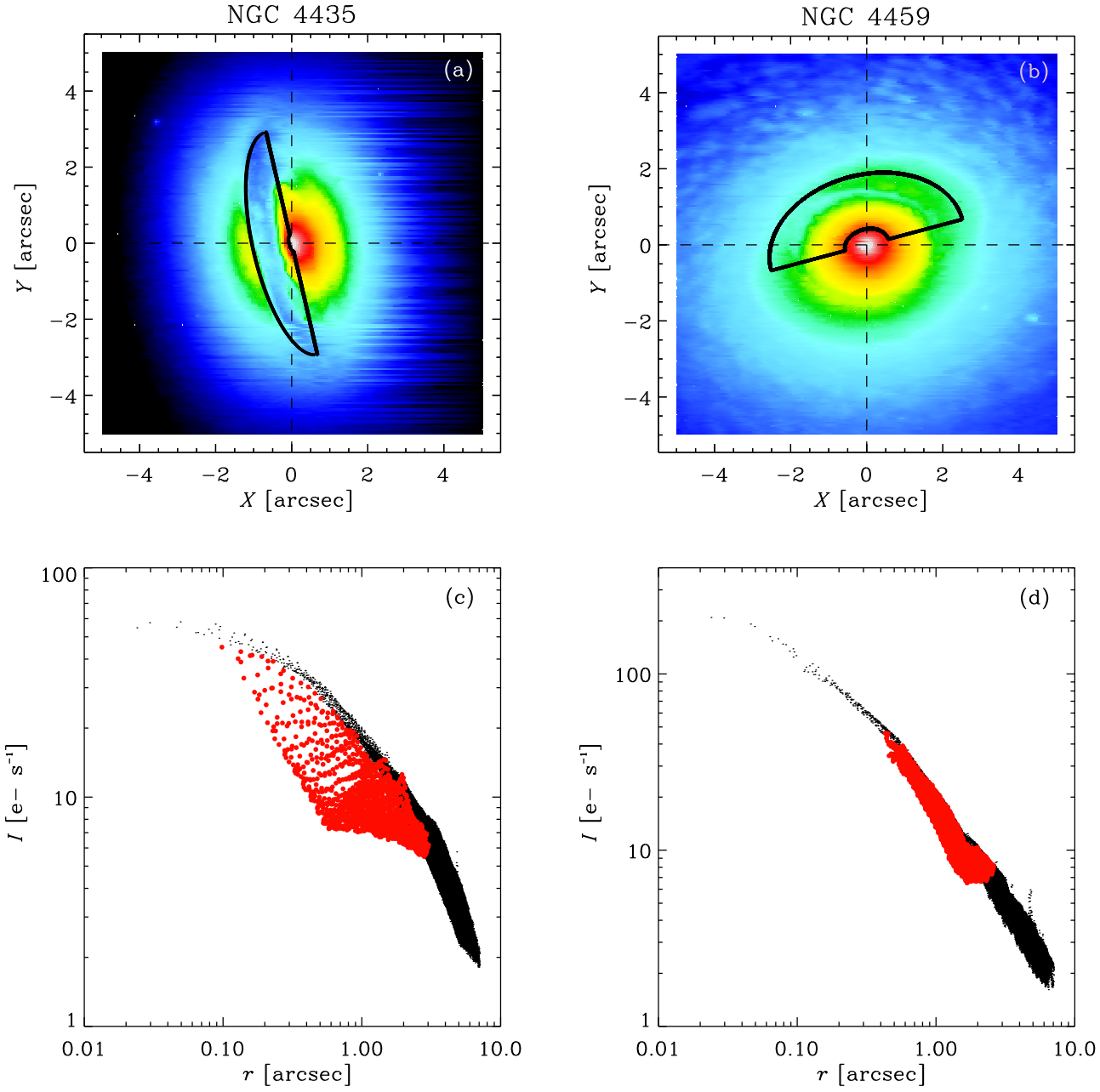

Figure 5. *Left-hand panels*: Central portion of the F850LP image of NGC 4435 with the contour (black thick line) of the adopted mask (*top panel*) and surface brightness of the masked (red filled circles) and unmasked pixels (black dots) as a function of their distance from the galaxy centre (*bottom panel*). The F850LP image is oriented with north at the top and east to the left and the field of view is 5″ × 5″. The dashed lines mark the galaxy centre. *Right-hand panels*: Same as above, but for NGC 4459.

allows for a simple reconstruction of the intrinsic surface brightness distribution (provided that the PSF can be approximated as a sum of Gaussian components) and to a straightforward deprojection of the intrinsic surface brightness into the luminosity volume density (which can also be expressed as the sum of a set of Gaussian components too).

Before using the MGE program we performed a photometric analysis in order to estimate the centre and position angle of both galaxies. For this we run `ellipse` task in IRAF after masking out the remaining foreground stars and background galaxies in the ACS images and inspected the results for the azimuthally averaged surface brightness, ellipticity, position angle, and centre coordinates. In particular, we found no evidence of a varying centre within the errors and calculated the mean position angle by averaging the values measured between 3″ and 6″ for NGC 4435 and between 3″ and 5″ for NGC 4459.

We then obtained an MGE best-fitting model to the galaxy surface brightness by keeping constant the centre and position angle of the Gaussians and while further restricting the range of the resulting axial ratios of the Gaussian components but keeping the fit acceptable, as described in Scott et al. (2013). This ensured that the permitted galaxy inclinations were not limited to a narrower range than that allowed by the data. We looked for the MGE best-fitting model by using different values of the position angle within 10°

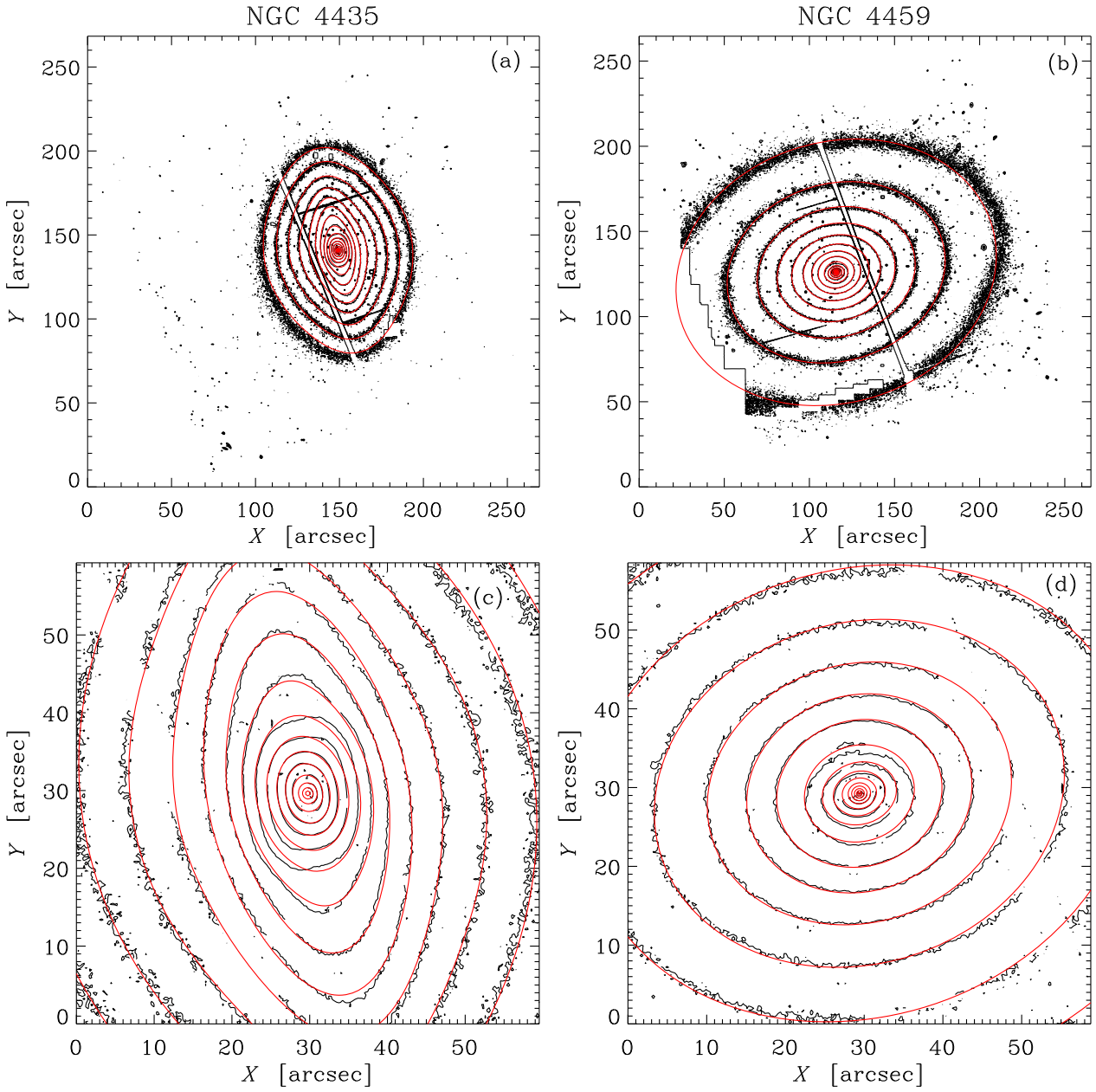

Figure 6. *Left-hand panels*: A few reference isophotes for the F850LP image (black lines) and MGE model (red lines) of NGC 4435. The entire field of view (*top panel*) and the central $1' \times 1'$ portion (*bottom panel*) of the image are shown. The image is oriented with north at the top and east to the left. Flux levels are normalized to the central surface brightness of the image and the contours are spaced by 0.5 mag arcsec^{-2}. While the MGE model was constrained using the original image, the image shown here is binned by 6×6 pixels to reduce the noise for comparison purposes only. The gap between the two WFC CCDs and a few bad rows are clearly visible, whereas missing portions of the galaxy isophotes correspond to masked regions. *Right-hand panels*: Same as above, but for NGC 4459.

from the guess value we obtained from the isophotal fitting. In the fitting process, we used the MGE model of the synthetic F850LP image of the PSF, which we generated with the TINYTIM package (Krist, Hook & Stoehr 2011).

In Fig. 6 we show the F850LP images of NGC 4435 and NGC 4459 at two different scales with a few representative galaxy isophotes and compare these to their MGE best-fitting models. We modelled the surface brightness radial profile of NGC 4459 as R^{-1} at large radii, where Savorgnan & Graham (2016) reported the presence of an exponential disc.

4.6 Jeans axisymmetric dynamical models

With the MGE models at hand, we proceeded to use the JAM IDL algorithm (Cappellari 2008) to build Jeans axisymmetric dynamical models for NGC 4435 and NGC 4459 in order to test the usefulness of our nuclear σ_* measurements in constraining the $M_\bullet$ of these objects. In particular we aimed at anchoring these models by matching the JAM predictions for the stellar $V_{\rm rms} = \sqrt{v_*^2 + \sigma_*^2}$ to the SAURON stellar kinematic measurements of Krajnović et al. (2011) and then to obtain from such best-fitting JAM models a

nuclear $V_{\rm rms}(0)$ value at the *HST* spatial resolution that can be directly compared to our STIS σ_* measurements.

To begin with, we built a set of mass-follows-light models by assuming that the mass volume density follows the luminosity volume density derived from the MGE fit and the deprojection of the galaxy surface brightness. These models have three free parameters that are optimized while matching the observed $V_{\rm rms}$. They are the dynamical mass-to-light ratio $(M/L)_{\rm dyn}$, the galaxy inclination i, and the anisotropy parameter $\beta_z = 1 - \sigma_z^2/\sigma_R^2$, where σ_R and σ_z are the radial and vertical components of the velocity dispersion, respectively, in a cylindrical coordinate system with the origin in the centre of the galaxy and symmetry axis aligned with its rotation axis. To build such models, we took advantage of the 2D maps of v_* and σ_* provided by the ATLAS^{3D} survey[3] (see Emsellem et al. 2004; Cappellari et al. 2011; McDermid et al. 2015, for all details). The integral-field spectroscopic data were obtained with SAURON working at William Herschel Telescope (Bacon et al. 2001) in low resolution mode with a field of view of about $30'' \times 40''$. The spatial scale per spaxel was $0\farcs8 \times 0\farcs8$ and the wavelength range between about 4800 and 5380 Å was covered with spectral resolution of $FWHM = 4.2$ Å corresponding to $\sigma_{\rm inst} = 108\ {\rm km\,s^{-1}}$. The observations were characterized by a typical seeing of $FWHM = 1\farcs5$. The data reduction and extraction of the stellar kinematics were presented in Cappellari et al. (2011), while the v_* and σ_* maps of NGC 4435 and NGC 4459 were shown in Krajnović et al. (2011), but see also Emsellem et al. 2004 for NGC 4459. We derived $V_{\rm rms}$ and corresponding errors from the available SAURON kinematics with no further modification.

For NGC 4435 the MGE results allowed only for inclination angles in excess of $i = 67^\circ$ when deprojecting the surface brightness, which is a limit that corresponds well with inclination $i = 70^\circ$ for the central ionized-gas disc as inferred by Coccato et al. (2006) from the dust lane morphology. For NGC 4459 we fixed the inclination by adopting the value of $i = 48^\circ$ from Cappellari et al. (2013), which also corresponds well to the $i = 47^\circ$ value for the central ionized-gas and dust disc measured by Sarzi et al. (2001). For both galaxies we then adopt radially constant values for both $(M/L)_{\rm dyn}$ and β_z, which were optimized by χ^2-minimization based on the $V_{\rm rms}$ measurements and associated errors. For NGC 4459, considering $\beta_z < 0$ would imply a lower χ^2/DOF, but for the fast rotators the assumption that $\beta_z \geq 0$ is observationally motivated (Cappellari 2008).

The best-fitting parameters of the mass-follows-light models of NGC 4435 were $(M/L)_{\rm dyn} = 2.18\ {\rm M_\odot/L_\odot}$, $\beta_z = 0.22$ and $i = 67^\circ$, while for NGC 4459 we found $(M/L)_{\rm dyn} = 1.66\ {\rm M_\odot/L_\odot}$ and $\beta_z = 0.00$ best-fitting values with $i = 48^\circ$. By construction these mass-follows-light dynamical models do not include an SBH, so we also constructed a second set of models including an SBH with $M_\bullet$ as predicted by the $M_\bullet - \sigma_{\rm e}$ relation of Kormendy & Ho (2013) and considering the $\sigma_{\rm e}$ values given by Cappellari et al. (2013), that is, $M_\bullet = 9.5 \times 10^7$ and $1.1 \times 10^8\ {\rm M_\odot}$ for NGC 4435 and NGC 4459, respectively. With these $M_\bullet$ values the JAM best-fitting parameters for NGC 4435 were $(M/L)_{\rm dyn} = 2.15\ {\rm M_\odot/L_\odot}$, $\beta_z = 0.21$, and $i = 67^\circ$, while for NGC 4459 we found $(M/L)_{\rm dyn} = 1.65\ {\rm M_\odot/L_\odot}$ and $\beta_z = 0.00$ with $i = 48^\circ$. Unsurprisingly, these are very similar to the $M_\bullet = 0$ models given that ground-based data generally do not provide much leverage on $M_\bullet$ measurements at the distance of these galaxies.

[3]The ATLAS^{3D} data are available at http://www-astro.physics.ox.ac.uk/atlas3d/.

The comparison between the SAURON $V_{\rm rms}$ maps of NGC 4435 and NGC 4459 and JAM prediction including an SBH are shown in Fig. 7. Although the models broadly compare well with the data in these maps, formally the JAM models are not good since they lead to reduced-χ^2 values around 2.8 and 2.5, for NGC 4435 and NGC 4459, respectively. As typical errors for the JAM best-fitting parameters we therefore adopted the estimates that Lablanche et al. (2012) obtained on the basis of simulations for early-type barred and unbarred galaxies, which correspond to errors smaller than 5° for the inclination, smaller than 0.15 for $(M/L)_{\rm dyn}$, and smaller than 0.3 for β_z. A comparison between our best-fitting values and those of the models of Cappellari et al. (2013) is not possible as the latter do not provide their β_z values.

Fig. 8 further illustrates how the JAM models compare to the SAURON measurements by showing major-axis $V_{\rm rms}$ profiles for both data and models within a $0\farcs8$-wide slit. Fig. 8 shows both models with $M_\bullet = 0\ {\rm M_\odot}$ and $M_\bullet$ from the $M_\bullet - \sigma_{\rm e}$ relation, which allows to better appreciate how these models differ by less than $10\ {\rm km\,s^{-1}}$ in the central regions, as expected for models tailored to match ground-based observations of limited spatial resolution. The large discrepancy between data and models seen between about $1''$ and $3''$ for NGC 4435 is due to the two-lobes structure of the SAURON $V_{\rm rms}$ map, which is quite difficult to reproduce (Fig. 7).

Having anchored the JAM models to match the SAURON data, we finally obtained the radial profiles of $V_{\rm rms}$ along the major axis of both galaxies by simply changing the spatial resolution and spatial sampling of the JAM models with $M_\bullet = 0\ {\rm M_\odot}$ and $M_\bullet$ from the $M_\bullet - \sigma_{\rm e}$ relation to match that of *HST*/STIS observations (Fig. 8). As expected, the profiles at ground-based and *HST* resolution begin to differ only in the inner $1''$, with a maximum difference of about $35\ {\rm km\,s^{-1}}$ in the centre in both the cases of NGC 4435 and NGC 4459. This allowed a direct comparison with values of $\sigma_{*,\rm fix}$ we measured from STIS spectra, which are also shown in Fig. 8.

For NGC 4435 the STIS $\sigma_{*,\rm fix} = 87.3^{+10.2}_{-8.8}\ {\rm km\,s^{-1}}$ is much smaller than the model prediction, at the *HST* resolution, of $V_{\rm rms}(0) = 185.3\ {\rm km\,s^{-1}}$ for $M_\bullet = 9.5 \times 10^7\ {\rm M_\odot}$. In fact, our nuclear σ_* value is even much smaller than the JAM prediction for $M_\bullet = 0\ {\rm M_\odot}$. On the other hand the STIS $\sigma_{*,\rm fix} = 214.6^{+11.2}_{-12.0}\ {\rm km\,s^{-1}}$ of NGC 4459 is almost consistent within the 1σ errors with the model prediction $V_{\rm rms}(0) = 199.1\ {\rm km\,s^{-1}}$ for $M_\bullet = 1.1 \times 10^8\ {\rm M_\odot}$.

Even though our reference JAM models are clearly somehow simplistic, in particular since they are based on the common assumption of constant vertical anisotropy profile and also in light of their limited ability to match the SAURON data in detail, we consider it unlikely that more sophisticated models for NGC 4435 will be able to predict nuclear σ_* values as low as those that we observe. For instance, to match the STIS $\sigma_{*,\rm fix}$ alone we would currently need rather extreme vertical anisotropy β_z values of about -0.9. More mild β_z variations, on the other hand, may help bridging the gap between the STIS measurements and the JAM model predictions in the case of NGC 4459.

5 CONCLUSIONS

We considered all the STIS spectra obtained with the G750M grating and bracketing the Hα line available in the Hubble Data Archive and which were placed on the nucleus of a galaxy, in order to obtain stellar velocity dispersion measurements within sub-arcsecond apertures. In this way, we arrived at a sample of 28 relatively nearby galaxies ($D < 70$ Mpc, see Table 1), spanning a wide range of morphological types (from E to Scd), central nuclear activity (Seyfert 2, LINERs, H II nuclei) and nuclear stellar velocity dispersion mea-

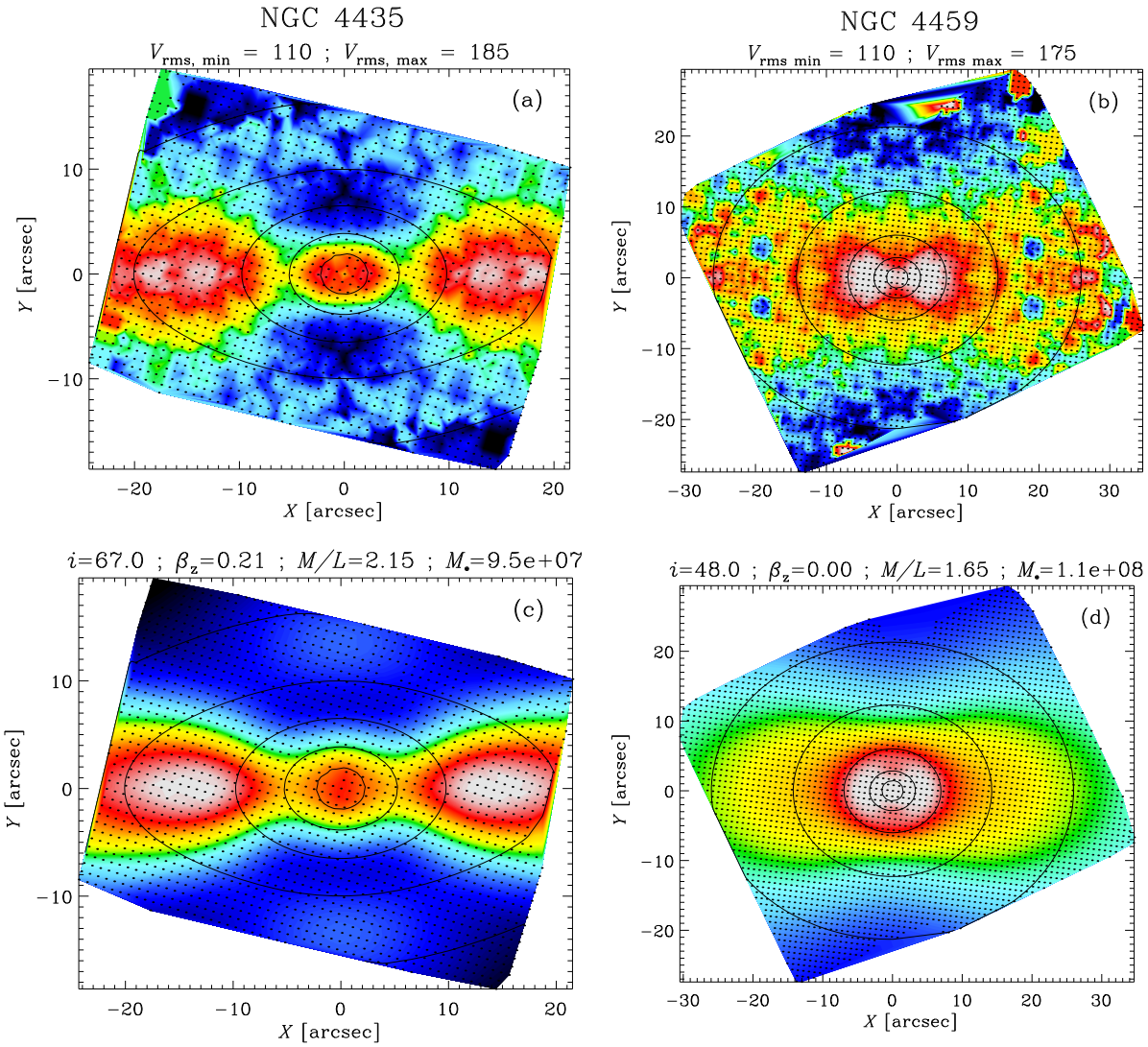

Figure 7. *Left-hand panels*: Comparison between $V_{\rm rms}$ from the SAURON stellar kinematics (*top panel*) and second velocity moment from JAM model (*bottom panel*) of NGC 4435. While the models were constrained using the original kinematics, the symmetrized $V_{\rm rms}$ map and bisymmetric JAM map are shown here for comparison purposes only. The minimum and maximum values of $V_{\rm rms}$ corresponding to black and white levels in the colour table are given on top of the SAURON map. The best-fitting parameters of the stellar dynamical model are shown on top of the JAM map. A few reference isophotes for the MGE model of F850LP image are also plotted with the galaxy major axis parallel to the horizontal axis. *Right-hand panels*: Same as above, but for NGC 4459.

surements ($50 < \sigma_* < 270\,{\rm km\,s^{-1}}$). For these objects, we extracted the stellar kinematics by matching the nuclear STIS spectra using the single-age, single-metallicity stellar population models of Vazdekis et al. (2010) and both narrow and broad Gaussian emission lines. For 24 objects we further constrained such a fit by using the optimal template from a similar fit to the G430L low-resolution STIS spectra that were also available for these galaxies, thus effectively fixing the stellar population mix while matching the G750M spectra. The good agreement between the nuclear σ_* values obtained with and without using such additional information, and additionally with the G750M σ_* measurements of Batcheldor et al. (2013) in the Ca II triplet near-infrared wavelength region, gave us further confidence in the σ_* measurements for the four galaxies for which we could only rely on the G750M spectra.

To start investigating the usefulness of such nuclear σ_* measurements in constraining $M_\bullet$ in nearby galaxies we then considered the case of NGC 4435 and NGC 4459, since these indeed appear to have quite different values of $M_\bullet$ from ionized-gas kinematical measurements despite showing similar ground-based $\sigma_{\rm e}$ values. Indeed, while NGC 4459 shows an $M_\bullet$ value consistent with the $M_\bullet - \sigma_\star$ relation (Sarzi et al. 2001), the $M_\bullet$ of NGC 4435 falls significantly below it (Coccato et al. 2006). Furthermore, these two galaxies feature quite different nuclear σ_* values in our catalogue, with NGC 4435 displaying a particularly lower σ_* value compared to NGC 4459 that could support the finding of Coccato et al. (2006).

We looked into this puzzle by building Jeans axisymmetric stellar dynamical models for NGC 4435 and NGC 4459 starting from archival ACS images and while matching the available integral-field SAURON stellar kinematics. In addition, in these models we adopted either $M_\bullet = 0\ {\rm M}_\odot$ or the $M_\bullet$ value from the $M_\bullet - \sigma_{\rm e}$ relation, which allowed us to predict the $V_{\rm rms}(0) \simeq \sigma_*$ by mimicking the *HST* spatial resolution and sampling, while essentially holding to JAM the values for stellar mass-to-light ratio, inclination, and anisotropy parameter that best matched the ground-based

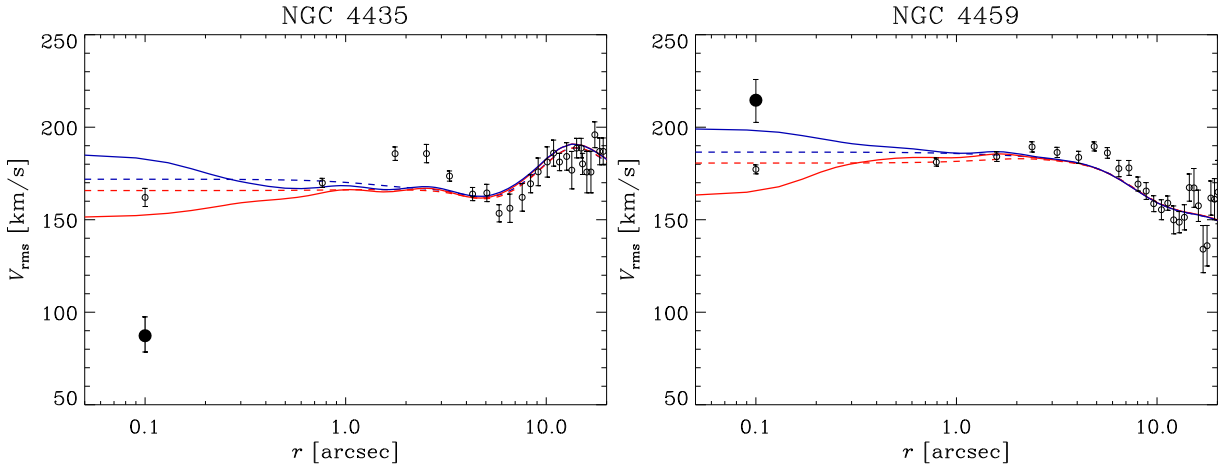

Figure 8. *Left-hand panels*: Comparison between the SAURON $V_{\rm rms}$ (black open circles) and second velocity moment from JAM best-fitting models with $M_\bullet = 0\ {\rm M}_\odot$ (red lines) and $M_\bullet = 9.5 \times 10^7\ {\rm M}_\odot$ (blue lines) along the major axis of NGC 4435. The dashed and continuous lines correspond to the JAM predictions for the SAURON and *HST* spatial resolution and sampling, respectively. The black filled circle corresponds to the sub-arcsecond $\sigma_{*,\,\rm fix}$ measured from the G750M spectrum. The central SAURON $V_{\rm rms}$ and G750M $\sigma_{*,\,\rm fix}$ are shifted to 0.″1 for comparison purposes only. *Right-hand panels*: Same as above, but for NGC 4459 with $M_\bullet = 0\ {\rm M}_\odot$ (red lines) and $M_\bullet = 1.1 \cdot 10^8\ {\rm M}_\odot$ (blue lines).

kinematics (see Section 4.6). In the case of NGC 4459 our nuclear σ_* value ($\sigma_{*,\rm fix} = 214.6^{+11.2}_{-12.0}$ km s^{-1}) was nearly consistent with the high-spatial resolution prediction for $V_{\rm rms}(0)$ at the $M_\bullet$ value given by the $M_\bullet - \sigma_{\rm e}$ relation ($V_{\rm rms}(0) = 199.1$ km s^{-1}), whereas for NGC 4435 the nuclear σ_* value ($\sigma_{*,\rm fix} = 87.3^{+10.2}_{-8.8}$ km s^{-1}) falls significantly below the model predictions even for $M_\bullet = 0\ {\rm M}_\odot$ ($V_{\rm rms}(0) = 151.6$ km s^{-1}).

Although our models are somehow simplistic, these results lend further support to the idea that the SBH of NGC 4435 is a genuine low outlier in the $M_\bullet - \sigma_{\rm e}$ relation, which deserves further investigation. For instance NGC 4435 would be an ideal target for future near-infrared observations from either space (e.g. with JWST) or from the ground while being assisted by adaptive optics (AO), such as those presented by Krajnović et al. (2018), who indeed also found evidence for undermassive SBH in two nearby early-type galaxies. AO assisted integral-field observations would also allow to establish if our nuclear σ_* dip can be explained by the presence of a central dynamically cold component such as a nuclear disc, although we note that in that case the presence of an SBH would be betrayed by an increased central stellar rotation (as also discussed by Krajnović et al. 2018). Theoretical works indicate that assessing the fraction of undermassive black holes in nearby galaxies would be quite important to constrain the processes driving the mass growth of SBHs and how they settled in galactic nuclei (Volonteri et al. 2011).

ACKNOWLEDGEMENTS

We acknowledge the anonymous referee. We are also grateful to John Magorrian, Bradley M. Peterson, and Sébastien Viaene for their valuable comments. IP is supported by Fondazione Cassa di Risparmio di Padova e Rovigo (Cariparo) through the 2015 Ph.D. fellowship 'Accurate mass determination of supermassive black holes in nearby galaxies'. EMC, EDB, LM, and AP acknowledge financial support from Padua University through grants DOR1699945/16, DOR1715817/17, DOR1885254/18, and BIRD164402/16. IP acknowledges the Centre for Astrophysics Research of the University of Hertfordshire, EMC and EDB acknowledge the Space Telescope Science Institute, and MS and BP acknowledge the Institut d'Astrophysique de Paris for the hospitality while this paper was in progress. This research is based on observations made with the NASA/ESA Hubble Space Telescope, and obtained from the Hubble Legacy Archive (http://hla.stsci.edu/), which is a collaboration between the Space Telescope Science Institute (STScI/NASA), the Space Telescope European Coordinating Facility (ST-ECF/ESA), and the Canadian Astronomy Data Centre (CADC/NRC/CSA). This research made use of data from the Hubble Data Archive through the Mikulski Archive for Space Telescopes (https://archive.stsci.edu/hst/) and of the NASA/IPAC Extragalactic Database (http://ned.ipac.caltech.edu/).

REFERENCES

Bacon R. et al., 2001, MNRAS, 326, 23
Batcheldor D., Axon D., Valluri M., Mandalou J., Merritt D., 2013, AJ, 146, 67
Beifiori A., Sarzi M., Corsini E. M., Dalla Bontà E., Pizzella A., Coccato L., Bertola F., 2009, ApJ, 692, 856
Beifiori A., Courteau S., Corsini E. M., Zhu Y., 2012, MNRAS, 419, 2497
Binggeli B., Sandage A., Tammann G. A., 1985, AJ, 90, 1681
Cappellari M., 2002, MNRAS, 333, 400
Cappellari M., 2008, MNRAS, 390, 71
Cappellari M., Emsellem E., 2004, PASP, 116, 138
Cappellari M. et al., 2007, MNRAS, 379, 418
Cappellari M. et al., 2011, MNRAS, 413, 813
Cappellari M. et al., 2013, MNRAS, 432, 1709
Coccato L., Sarzi M., Pizzella A., Corsini E. M., Dalla Bontà E., Bertola F., 2006, MNRAS, 366, 1050
Cortese L., Bendo G. J., Isaak K. G., Davies J. I., Kent B. R., 2010, MNRAS, 403, L26
Cretton N., van den Bosch F. C., 1999, ApJ, 514, 704
de Vaucouleurs G., de Vaucouleurs A., Corwin H. G., Jr., Buta R. J., Paturel G., Fouqué P., 1991 , Third Reference Catalogue of Bright Galaxies. Springer-Verlag, Berlin
Dressel L., Holfeltz S., Quijano J. K., 2007, STIS Data Handbook. Version 5.0. STScI, Baltimore
Emsellem E., Monnet G., Bacon R., 1994, A&A, 285, 723
Emsellem E. et al., 2004, MNRAS, 352, 721
Falcón-Barroso J., Sánchez-Blázquez P., Vazdekis A., Ricciardelli E., Cardiel N., Cenarro A. J., Gorgas J., Peletier R. F., 2011, A&A, 532, A95

Falcón-Barroso J. et al., 2017, A&A, 597, A48
Ferrarese L. et al., 2006, ApJS, 164, 334
Gonzaga S. et al., 2012, The DrizzlePac Handbook. Version 1.0. STScI, Baltimore
Graham A. W., 2016, in Laurikainen E., Peletier R., Gadotti D., eds, Astrophysics and Space Science Library Vol. 418, Galactic Bulges, Springer International Publishing Switzerland, Cham (Germany), p. 263
Gültekin K., Richstone D. O., Gebhardt K., Faber S. M., Lauer T. R., Bender R., Kormendy J., Pinkney J., 2011, ApJ, 741, 38
Ho L. C., Filippenko A. V., Sargent W. L. W., 1997, ApJS, 112, 315
Kenney J. D. P., Tal T., Crowl H. H., Feldmeier J., Jacoby G. H., 2008, ApJ, 687, L69
Kormendy J., Ho L. C., 2013, ARA&A, 51, 511
Kormendy J. et al., 1997, ApJ, 482, L139
Kormendy J., Fisher D. B., Cornell M. E., Bender R., 2009, ApJS, 182, 216
Krajnović D., Jaffe W., 2004, A&A, 428, 877
Krajnović D. et al., 2011, MNRAS, 414, 2923
Krajnović D. et al., 2018, MNRAS, 477, 3030
Krist J. E., Hook R. N., Stoehr F., 2011, in Kahan M. A., ed., Optical Modeling and Performance Predictions V. SPIE, Bellingham, p. 81270J
Kuntschner H. et al., 2010, MNRAS, 408, 97
Lablanche P.-Y. et al., 2012, MNRAS, 424, 1495
Lucas R. A. et al., 2016, ACS Instrument Handbook. Version 8.0. STScI, Baltimore
McDermid R. M. et al., 2015, MNRAS, 448, 3484
Nelder J. A., Mead R., 1965, Comput. J., 7, 308
Nowak N., Saglia R. P., Thomas J., Bender R., Davies R. I., Gebhardt K., 2008, MNRAS, 391, 1629
Pagotto I. et al., 2017, Astron. Nachr., 338, 841
Pavlovsky C. et al., 2004, , , , in ACS Instrument Handbook. Version 5.0, STScI, (Baltimore: ,), .
Riley A. et al., 2017, STIS Instrument Handbook, Version 16.0. STScI, Baltimore
Saglia R. P. et al., 2016, ApJ, 818, 47
Sánchez-Blázquez P. et al., 2006, MNRAS, 371, 703
Sani E., Marconi A., Hunt L. K., Risaliti G., 2011, MNRAS, 413, 1479
Sarzi M., Rix H. W., Shields J. C., Rudnick G., Ho L. C., McIntosh D. H., Filippenko A. V., Sargent W. L. W., 2001, ApJ, 550, 65
Sarzi M. et al., 2002, ApJ, 567, 237
Sarzi M., Rix H. W., Shields J. C., Ho L. C., Barth A. J., Rudnick G., Filippenko A. V., Sargent W. L. W., 2005, ApJ, 628, 169
Sarzi M. et al., 2006, MNRAS, 366, 1151
Savorgnan G. A. D., Graham A. W., 2015, MNRAS, 446, 2330
Savorgnan G. A. D., Graham A. W., 2016, ApJS, 222, 10
Schlafly E. F., Finkbeiner D. P., 2011, ApJ, 737, 103
Scott N. et al., 2013, MNRAS, 432, 1894
Shankar F. et al., 2016, MNRAS, 460, 3119
van den Bosch R. C. E., 2016, ApJ, 831, 134
van den Bosch R. C. E., Gebhardt K., Gültekin K., van de Ven G., van der Wel A., Walsh J. L., 2012, Nature, 491, 729
van den Bosch R. C. E., Gebhardt K., Gültekin K., Yıldırım A., Walsh J. L., 2015, ApJS, 218, 10
van Dokkum P. G., 2001, PASP, 113, 1420
Vazdekis A., Sánchez-Blázquez P., Falcón-Barroso J., Cenarro A. J., Beasley M. A., Cardiel N., Gorgas J., Peletier R. F., 2010, MNRAS, 404, 1639
Verdoes Kleijn G. A., van der Marel R. P., de Zeeuw P. T., Noel-Storr J., Baum S. A., 2002, AJ, 124, 2524
Vika M., Driver S. P., Cameron E., Kelvin L., Robotham A., 2012, MNRAS, 419, 2264
Vollmer B., Braine J., Combes F., Sofue Y., 2005, A&A, 441, 473
Volonteri M., Natarajan P., Gültekin K., 2011, ApJ, 737, 50
Walsh J. L., van den Bosch R. C. E., Gebhardt K., Yildirim A., Gültekin K., Husemann B., Richstone D. O., 2015, ApJ, 808, 183
Walsh J. L., van den Bosch R. C. E., Gebhardt K., Yıldırım A., Gültekin K., Husemann B., Richstone D. O., 2017, ApJ, 835, 208

This paper has been typeset from a TEX/LATEX file prepared by the author.